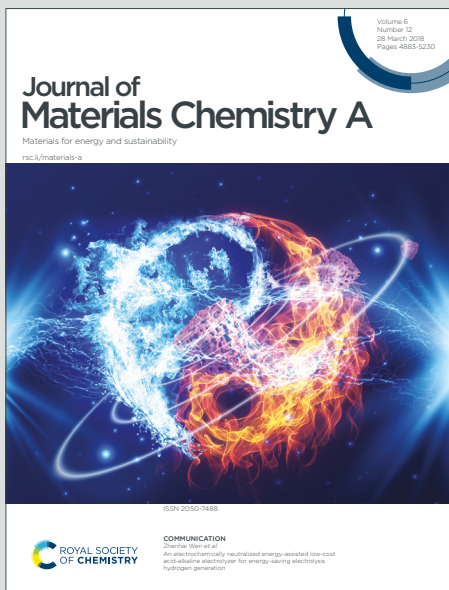


Journal of Materials Chemistry A

Materials for energy and sustainability

Accepted Manuscript

This article can be cited before page numbers have been issued, to do this please use: J. Wang, A. A. Panchal, G. Sai Gautam and P. Canepa, *J. Mater. Chem. A*, 2022, DOI: 10.1039/D2TA02202H.



This is an Accepted Manuscript, which has been through the Royal Society of Chemistry peer review process and has been accepted for publication.

Accepted Manuscripts are published online shortly after acceptance, before technical editing, formatting and proof reading. Using this free service, authors can make their results available to the community, in citable form, before we publish the edited article. We will replace this Accepted Manuscript with the edited and formatted Advance Article as soon as it is available.

You can find more information about Accepted Manuscripts in the [Information for Authors](#).

Please note that technical editing may introduce minor changes to the text and/or graphics, which may alter content. The journal's standard [Terms & Conditions](#) and the [Ethical guidelines](#) still apply. In no event shall the Royal Society of Chemistry be held responsible for any errors or omissions in this Accepted Manuscript or any consequences arising from the use of any information it contains.

Journal Name

ARTICLE TYPE

Cite this: DOI: 00.0000/xxxxxxxxxx

Received Date
Accepted Date

DOI: 00.0000/xxxxxxxxxx

The Resistive Nature of Decomposing Interfaces of Solid Electrolytes with Alkali Metal Electrodes[†]

Juefan Wang,^a Abhishek A. Panchal,^a Gopalakrishnan Sai Gautam,^b Pieremanuele Canepa^{a,c*}

A crucial ingredient in lithium (Li) and sodium (Na)-ion batteries (LIBs and NIBs) is the electrolytes. The use of Li-metal (Na-metal) as anode in liquid electrolyte LIBs (NIBs) is constrained by several issues including thermal runaway and flammability, electrolyte leakage, and limited chemical stability. Considerable effort has been devoted toward the development of solid electrolytes (SEs) and all-solid-state batteries, which are presumed to mitigate some of the issues of Li-metal(Na-metal) in contact with flammable liquid electrolytes. However, most SEs, such as Li_3PS_4 , $\text{Li}_6\text{PS}_5\text{Cl}$ and Na_3PS_4 readily decompose against the highly reducing Li-metal and Na-metal anodes. Using first-principles calculations we elucidate the stability of more than 20 solid||solid interfaces formed between the decomposition products of Li_3PS_4 , $\text{Li}_6\text{PS}_5\text{Cl}$ (and Na_3PS_4) against the Li-metal (Na-metal) electrode. We suggest that the work of adhesion needed to form a heterogeneous interfaces is an important descriptor to quantify the stability of interfaces. Subsequently, we clarify the atomistic origins of the resistance to Li-ion transport at interfaces of the Li-metal anode and selected decomposition products (Li_3P , Li_2S and LiCl) of SEs, via a high-fidelity machine learned potential (MLP). Utilising an MLP enables nano-second-long molecular dynamics simulations on 'large' interface models (here with 8320 atoms), but with similar accuracy to first-principles approaches. Our simulations demonstrate that the interfaces formed between Li-metal and argyrodite (e.g., $\text{Li}_6\text{PS}_5\text{Cl}$) decomposition products are resistive to Li-ion transport. The implications of this study are important since binary compounds are commonly found in the vicinity of Li(Na)-metal upon chemical and/or electrochemical decomposition of ternary and quaternary SEs.

1 Introduction

Rechargeable lithium-ion batteries (LIBs) keep gaining importance for the development of the next-generation energy storage devices and electric vehicles because of their outstanding gravimetric and volumetric energy densities.^{1–5} Lithium metal batteries (LMBs) utilizing Li-metal anodes —that can achieve unprecedented energy densities theoretically, as compared to LIBs— have become one of the central topics of current research in rechargeable batteries.^{4–6} The primary challenge in constructing practical LMBs is stabilizing the Li-metal|electrolyte interface, with scientific studies mostly focused on identifying electrolyte formulations with limited reactivity and/or suitable additives.^{1,5,7} Stabilizing the metal|electrolyte interface is also a bottleneck in developing Na-metal batteries (NMBs).^{4,5,8–10}

Solid electrolytes (SEs) are critical components in the develop-

ment of LMBs and solid-state LIBs.^{11–18} Besides acting as separators between electrodes, SEs are also expected to alleviate some of the safety issues between Li-metal anodes and liquid electrolytes.^{4,5,19} Nevertheless, numerous reports have demonstrated high electrochemical instabilities of SEs when in contact with Li-metal anode (and other electrode materials).⁴ For example, sulfur-containing SEs are unstable against Li-metal, resulting in the formation of undesired decomposition products, which may resist Li-ion transport and/or facilitate electron transport.^{12–15,20–22} Thus, the stabilization of interfaces formed between Li-metal (or other alkali-metal electrodes) and SEs remains a significant bottleneck in designing practical solid-state batteries.

Electrolyte decomposition occurs at small length scales away from the exteriors of the cell packs that constitute a battery. Therefore, the characterization of decomposition products in fully assembled and operating devices requires dedicated custom-made and expensive tools.^{13,14,23,24} A number of reports have analyzed the compositions, structures, and formation mechanisms of the decomposing products of SEs against metal electrodes (metal electrode || SE).^{12–15,20–22} For example, X-ray photoemission spectroscopy (XPS) experiments by Wenzel *et al.*¹⁴ reported

^aDepartment of Materials Science and Engineering, National University of Singapore, 9 Engineering Drive 1, Singapore 117575, Singapore. ^bDepartment of Materials Engineering, Indian Institute of Science, Bangalore 560012, India. ^cChemical and Biomolecular Engineering, National University of Singapore, 4 Engineering Drive 4, Singapore 117585. *E-mail: pcanepa@nus.edu.sg

† Electronic Supplementary Information (ESI) available



that $\text{Li}_6\text{PS}_5\text{X}$ (with X=Cl, Br and I), upon contact with Li-metal, forms Li_2S , LiX , and Li_3P . As a result, the decomposition products of metal electrode||SE interfaces are expected to be multiphased and highly heterogeneous, which complicates the description of ionic transport across interfaces. Furthermore, the structures and properties of the metal electrode||SE interfaces are expected to be markedly different from the bulk materials. A detailed study of the interfacial properties, particularly ionic transport, is needed for the advancement of solid-state batteries.

Another aspect of solid-state batteries relates to the mechanical stability (i.e., adhesion) of the solid||solid interfaces that are electrochemically formed. The loss of contact due to lack of adhesion between Li-metal and SEs appears as a major cause driving the buildup of interfacial impedance in solid-state devices.^{4,5,25} To evaluate the mechanical stabilities of the interfaces, Lepley and Holzwarth²⁶ have performed accurate first-principles calculations of several Li-metal||SE interfaces (such as, $\text{Li}||\text{Li}_2\text{O}$, $\text{Li}||\text{Li}_2\text{S}$, $\text{Li}||\text{Li}_3\text{PO}_4$ and $\text{Li}||\text{Li}_3\text{PS}_4$) and found that all interfaces were stable except $\text{Li}||\text{Li}_3\text{PS}_4$. Other studies have investigated the effects of stability of heterogeneous interfaces on the Li-ion transport properties.^{27–29}

Yang and Qi²⁷ have proposed that an interface with good adhesion, i.e. "lithiophilic interface" can result in a faster critical stripping current density, which is crucial to prevent dendrite growth. Recently, Seymour and Aguadero²⁸ have shown that Li (or Na)-ion transport across alkali-metal||SE interfaces correlates directly with the interfacial adhesion. Yang *et al.*²⁹ have employed classical molecular dynamics (MD) to study the process of Li plating and stripping on solid Li_2O , showing that a coherent interface with strong interfacial adhesion and fast Li-ion diffusion can prevent pore formation at the interface. Here, we perform a systematic investigation including a larger data set of solid||solid interfaces, particularly focusing on the correlation between the atomistic structure of interfaces and ionic transport, which is presently lacking.

We address the interfacial stability and Li-ion mobility of multiple interfaces formed between Li-metal electrode and decomposition products of topical SEs, such as, Li_3PS_4 ,^{15,26,30,31} argyrodite- $\text{Li}_6\text{PS}_5\text{Cl}$ ¹⁴ and LiPON, with the general formula $\text{Li}_x\text{PO}_y\text{N}_z$.^{23,24,32} We also analyze the $\text{Na}||\text{Na}_2\text{S}$ and $\text{Na}||\text{Na}_3\text{P}$ interfaces, which form upon the decomposition of Na_3PS_4 against Na-metal.¹³ We perform large-scale MD simulations of selected interfaces, (i.e., $\text{Li}||\text{Li}_3\text{P}$, $\text{Li}||\text{Li}_2\text{S}$ and $\text{Li}||\text{LiCl}$) based on high-fidelity machine learned potentials (MLPs) trained on accurate first-principles data, which carry the accuracy of *ab initio* molecular dynamics (AIMD) while giving access to appreciably larger time and length scale simulations.

We reveal that the mechanical stabilities of the Li (or Na)-metal||SE interfaces are primarily governed by the atomistic structures of the interfaces, which in turn are dependent on the surface orientations and/or terminations of the decomposition products. Further, we show that the interfaces formed between Li-metal and decomposition products of the argyrodite $\text{Li}_6\text{PS}_5\text{Cl}$ SE (i.e., Li_3P , Li_2S and LiCl) are resistive to Li-ion transport, explaining the observed impedance buildup. Our results provide insights to engineer solid||solid interfaces with better interfacial

stability and improved ionic transport.

2 Construction of Interfaces of Decomposition Products and Metal Anodes

We discuss the procedure to build heterogeneous interfaces between an alkali-metal (Li or Na) with one of their binary compounds (e.g., Li_3P), formed as a result of SE decomposition. In constructing the heterogeneous interfaces between the alkali-metal (e.g., Li or Na) and the binary compounds, we identify stable stoichiometric surfaces (following Tasker's criteria³³) with low surface energies, γ , of both materials, which are paired into an interface (see Table S1 of the Electronic Supplementary Information, ESI). To describe γ , we have used the slab model in Eq. 1.³⁴

$$\gamma = \lim_{N \rightarrow \infty} \frac{1}{2S} [E_{\text{slab}}^N - NE_{\text{bulk}}] \quad (1)$$

where S is the surface area of the slab, E_{slab}^N is the energy of the relaxed slab containing N formula units, and E_{bulk} is the energy per formula unit of the bulk structure. The energies of Eq. 1 (and the following equations) are Gibbs energies, which we approximated by density functional theory (DFT, see Sec. 7) total energies ignoring pV and entropic contributions. Slab models included sufficient number of layers and a vacuum of 15 Å were used to converge γ to within $\pm 0.01 \text{ J m}^{-2}$.

The set of stable surfaces in Li(or Na)-metal and binary compounds considered, and their corresponding γ , are displayed in the Wulff shapes of Figure 1.^{35,36} The values of γ , not shown in Figure 1, are included in Table S2-S3 of ESI. The (100) surface of Li-metal has the lowest surface energy of $\sim 0.46 \text{ J m}^{-2}$, while for Na-metal, the (100) and (110) surfaces have similar γ values, $\sim 0.22 \text{ J m}^{-2}$ and $\sim 0.21 \text{ J m}^{-2}$. In Li_2S , Li_2O , Na_2S , and Na_2O , the (111) facet dominates the Wulff shape, while for Li_3P , LiCl , Li_3N , and Na_3P , the {001}-type surfaces have the lowest γ values (Figure 1). Our calculated surface energies, $\sim 0.33 \text{ J m}^{-2}$ for the (111) surface and $\sim 0.51 \text{ J m}^{-2}$ for the (110) surface of Li_2S , as well as $\sim 0.53 \text{ J m}^{-2}$ for the (111) surface of Li_2O are consistent with the values reported by previous literatures.^{37,38} Li_3N and LiCl exhibit stable facets that are terminated with both Li and anion species, while other compounds have stable facets exposing a Li (or Na) layer.

The surfaces of Figure 1 are subsequently paired to form heterogeneous interfaces. Different metrics serve to quantify the effect of mechanical strain and/or the chemical bonds formation/destruction at the interface.^{39,40} The interface formation energy (E_f in Eq. 2) is the energy difference between the interface model and bulk structures of A and B, and includes both mechanical (i.e., elastic strain) and chemical components.³⁴

$$E_f = \frac{E_{AB} - [N_A E_A + N_B E_B]}{2S} \quad (2)$$

where S is the surface area of the interface, E_{AB} is the energy of the fully relaxed interface model, containing N_A and N_B formula units of materials A and B, whose bulk energies are E_A and E_B , respectively. Elastic stress can arise in interfaces displaying large lattice mismatch, and "absorbed" by the interface through the release of the stress energy, via formation of dislocations.^{41,42} By



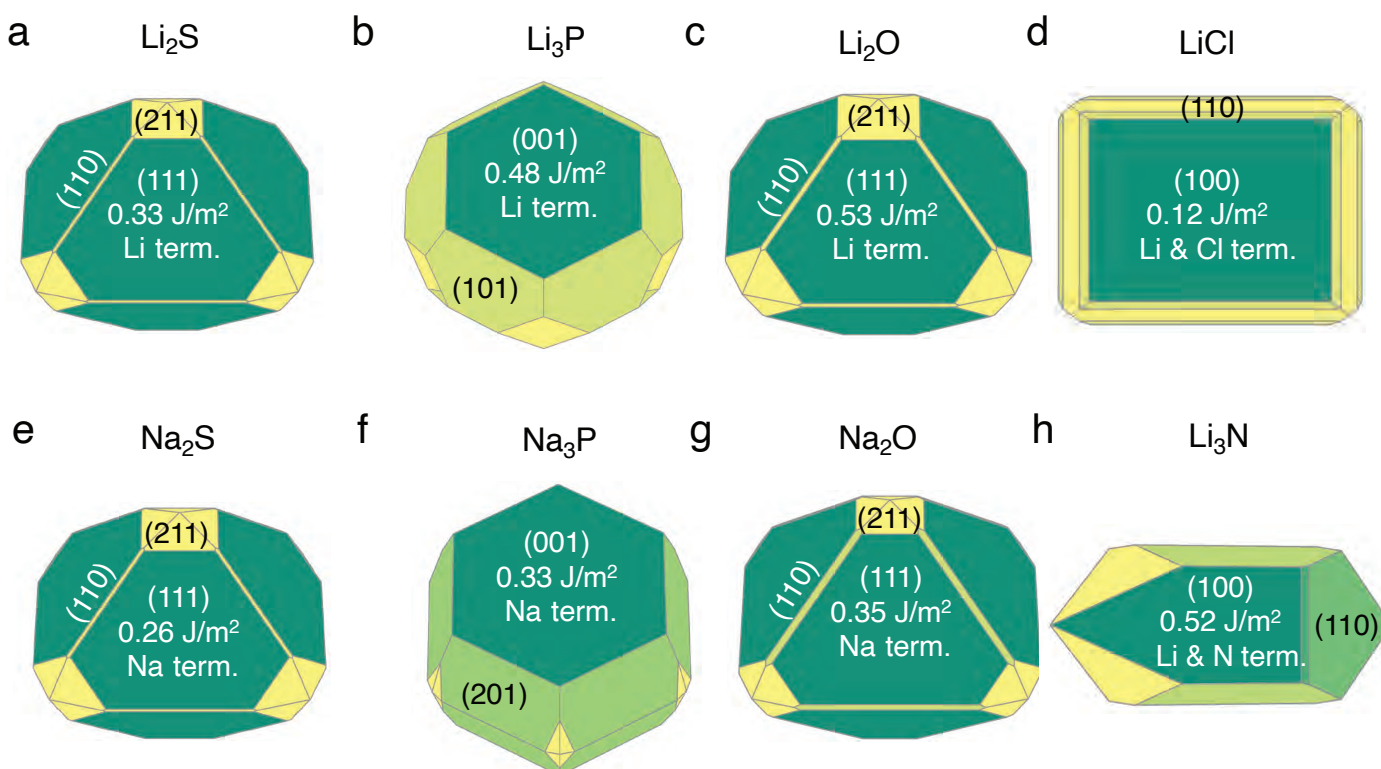


Fig. 1 Computed Wulff shapes of binary compounds Li₂S (panel a), Li₃P (b), Li₂O (c), LiCl (d), Na₂S (e), Na₃P (f), Na₂O (g), and Li₃N (h), with their corresponding surface energies (in J m⁻²). The chemical nature of the surface terminations (term.) are indicated. Wulff polygons are constructed using stoichiometric, non-polar, and symmetric (including an inversion symmetry) surfaces.

removing the elastic strain from E_f (of Eq. 2), we obtain two important descriptors: *i*) the interfacial energy, σ of Eq. 9, and *ii*) the work of adhesion, W_{adhesion} of Eq. 4, which are paramount in evaluating the overall stability of interfaces. σ quantifies the formation (or destruction) of chemical bonds as the interface is created, excluding all mechanical contributions.

$$\sigma = \frac{E_{AB} - [N_A E_{A(z)} + N_B E_{B(z)}]}{2S} \quad (3)$$

where $E_{A(z)}$ and $E_{B(z)}$ are the energy per formula unit of the bulk A and B , as obtained from a constrained relaxation along the normal direction (z) to the interface, where the in-plane lattice vectors of the bulk structures are fixed to those of the fully relaxed interface. It follows that, the elastic strain energy associated with the interface is calculated as $E_f - \sigma$.

The work of adhesion, W_{adhesion} (of Eq. 4) is the work done to part two adherent surfaces to an infinite distance, and quantifies the mechanical stability of an interface.

$$W_{\text{adhesion}} = \gamma_A + \gamma_B - \sigma \quad (4)$$

where γ_A and γ_B (Eq. 1) are the surface energies of materials A and B , respectively. Nominally small (positive) values of σ and large (positive) values of W_{adhesion} are indicative of a high interfacial stability. To account for the effect of elastic strain, Eq. 5 gives

an alternative definition of W_{adhesion} .

$$W_{\text{adhesion}} = \gamma_A + \gamma_B - E_f \quad (5)$$

For the creation of interface models, we use the algorithm by Taylor *et al.*,⁴³ which samples the configurational space to find interface models that minimize the lattice mismatch between two materials. While pairing surfaces, we used the in-plane lattice constants of the binary compounds (e.g., Li₃P) and applied a lattice mismatch-induced strain to the metal surface, since the bulk moduli of binary compounds are typically greater than the alkali-metals (i.e., Li and Na).^{11,44} The constructed interface models are symmetric; for example, Li₂S || Li-metal consists of two identical interfaces that forms a Li₂S || Li–metal || Li₂S system, as displayed in panel c in Figure 2. The slab thickness of binary compounds is typically ~10 Å, which is sufficient to distinguish the interface features from their bulk-like properties. However, thicker slabs are required for Li (~12 Å) and Na (~14 Å) to distinguish the interface regions from the bulk region.²⁶

3 Stability of Interfaces of Decomposition Products and Metal Electrodes

Figure 2a and b show the computed interfacial energetics, E_f , σ , and W_{adhesion} (as defined in Eq. 4), for a number of interfaces considered. An illustration of the interface models for Li(110) || Li₂S(110), Na(110) || Na₂S(110), Li(100) || Li₃P(001) and Na(100) || Na₃P(001) is shown in Figure 2c-f, where the in-

interfacial regions are indicated by the shaded areas. Representations of other interfaces are shown in Figure S1-S5 of ESI. In the Li cases considered, we find the most stable interfaces are those formed with Li_3N , displaying W_{adhesion} in the range of 0.8–1.0 J m⁻², and $\sigma \sim 0.25$ J m⁻² (Figure 2a). In contrast, the least stable interfaces are $\text{Li}||\text{LiCl}$, which exhibit low W_{adhesion} and high σ . In Na-based systems, the most and least stable interfaces are $\text{Na}(110)||\text{Na}_2\text{O}(110)$ and $\text{Na}(100)||\text{Na}_3\text{P}(001)$, respectively. Note that results of W_{adhesion} from Eq. 5 (including strain contributions) in Figure S7-S8 appear similar in magnitude (and sign) to those obtained with Eq. 4 (excluding strain) in Figure 2. Therefore, we will refer to W_{adhesion} of Eq. 4 and Figure 2 through the remainder of the manuscript.

Previous computational and experimental studies have suggested that $\text{Li}||\text{Li}_2\text{S}$, $\text{Li}||\text{Li}_3\text{P}$ and $\text{Li}||\text{LiCl}$ interfaces are expected to form when argyrodite- $\text{Li}_6\text{PS}_5\text{Cl}$ SE reacts with Li-metal.^{14,15} A comparison of W_{adhesion} (Figure 2a) of these interfaces indicates $\text{Li}||\text{LiCl} << \text{Li}||\text{Li}_2\text{S} < \text{Li}||\text{Li}_3\text{P}$. $\text{Li}(100)||\text{Li}_3\text{P}(001)$ is expected to dominate the overall interface of Li-metal and $\text{Li}_6\text{PS}_5\text{Cl}$, if similar quantities of Li_2S and Li_3P are produced upon decomposition. In the case of Li_3PS_4 , predicted values of W_{adhesion} (Figure 2a) suggest the coexistence of both $\text{Li}||\text{Li}_2\text{S}$ and $\text{Li}||\text{Li}_3\text{P}$ interfaces, consistent with prior literatures.^{15,45,46} For LiPON, W_{adhesion} follows the order $\text{Li}||\text{Li}_3\text{P} < \text{Li}||\text{Li}_2\text{O} \approx \text{Li}||\text{Li}_3\text{N}$, implying that the Li-metal anode will mostly interface with Li_2O and Li_3N , also consistent with previous investigations.^{15,23,24,32,47}

In most cases considered, the interfacial region (shaded regions in Figure 2c and d) exhibits substantial atomic rearrangements upon full relaxation, with the exceptions being $\text{Li}(110)||\text{Li}_3\text{N}(110)$ (Figure S3) and $\text{Li}(110)||\text{LiCl}(100)$ (Figure S2). A qualitative analysis of the interface models suggests that there is always a pronounced atomic reconstruction on the metal side of the interface as compared to that of the binary compound for all Li (and Na) interfaces. This is another confirmation that both Li and Na metals are softer than their binary compounds.⁴⁴ Li (or Na) atoms originating from the metal side of the interfacial region form stabilising bonds with anion species from the compound side, with bond lengths that are similar to the bulk binary structures (see Table S5).

In general, interfaces with lattice mismatch smaller than a few percent can be considered as epitaxial, and the re-organization of atoms at the interface remains minimal compared to others with significant lattice mismatch ($\geq 5\%$). In some cases, we find large lattice mismatches when interfaces are formed from the dominant facets of binary compounds with the (100) or (110) surfaces of the metals (Li or Na). For example, the $\text{Li}_2\text{S}(111)$ facet displays a lattice mismatch of $\sim 14.2\%$ with the $\text{Li}(100)$ surface (Table S3), indicating that such an interface may not occur practically. The lattice mismatch between $\text{Li}_2\text{S}(110)$ and $\text{Li}(110)$ facets is lower ($\sim 5.1\%$) and consequently exhibits higher W_{adhesion} than $\text{Li}_2\text{S}(111)||\text{Li}(100)$. The $\text{Li}_2\text{S}||\text{Li}$ interface is likely to exhibit significant structural re-arrangement since $\text{Li}_2\text{S}(110)$ facet does not occupy a significant portion of the Wulff volume of Li_2S , and consequently result in a $\text{Li}_2\text{S}||\text{Li}$ interface that is susceptible to delamination in real devices.

We also find that the surface terminations of binary compounds

are crucial to determine the interfacial stability. For example, the $\text{Li}(110)||\text{Li}_2\text{O}(111)$ interface has a small lattice mismatch of $\sim 1.73\%$ (Table S3). However, its fully relaxed geometry exhibits larger lattice distortion of the interfacial region as compared to other $\text{Li}||\text{Li}_2\text{O}$ based interfaces (see Figure S4). This interfacial instability comes from the fact that the $\text{Li}_2\text{O}(111)$ surface is terminated with only Li atoms —this excess number of Li atoms and lack of anions near the interface region affects the chemical stabilization of the interface due to the lack the bond formation between Li (from the metal side of the interface) and O.

In Na systems, the $\text{Na}(110)||\text{Na}_2\text{S}(110)$, $\text{Na}(100)||\text{Na}_2\text{S}(111)$, and $\text{Na}(100)||\text{Na}_3\text{P}(001)$ show reconstructions in the interfacial region similar to their Li analogues (Figure 2c and Fig. S1c,d). Additionally, we find the computed values of W_{adhesion} (and σ) to be lower (less positive) than their corresponding Li analogues (see Figure 2a and b). Despite the low values of W_{adhesion} (< 0.35 J m⁻²), both $\text{Na}||\text{Na}_2\text{S}$ and $\text{Na}||\text{Na}_3\text{P}$ may still occur at the Na-metal electrode. The $\text{Na}||\text{Na}_2\text{O}$ interface has a significantly larger W_{adhesion} (~ 0.65 J m⁻²) than $\text{Na}||\text{Na}_3\text{P}$ (~ 0.35 J m⁻²) and $\text{Na}||\text{Na}_2\text{S}$ interfaces (~ 0.30 J m⁻²).

4 Lithium Transport at Heterogeneous Interfaces

To quantify ionic transport through heterogeneous interfaces, we have used the tracer diffusivity, D^* of Eqs. 6 and 7. While we quantify only Li-ion transport across heterogeneous interfaces, similar qualitative trends might hold for Na-ion transport as well.

$$D^*(T) = \lim_{t \rightarrow \infty} \frac{1}{2dt} \frac{1}{N} \sum_{i=1}^N \left\langle |r_i(t) - r_i(0)|^2 \right\rangle; \quad (6)$$

$$D^*(T) = D_0 \exp\left(-\frac{E_a}{k_B T}\right). \quad (7)$$

where $r_i(t)$ is the displacement of the i^{th} Li-ion at time t , N is the number of diffusing ions, and d is the dimensionality of the diffusion process. E_a in the Arrhenius Eq. 7 is the Li-ion migration energy, D_0 is the ionic diffusivity at infinite temperature (T), and k_B is the Boltzmann constant. We obtain D^* , D_0 and E_a from MD simulations based on our trained moment tensor potentials (MTPs),⁴⁸ which is machine learned from AIMD simulations of the bulk and interface structures (see Sec. 7.2). The largest MD simulations of heterogeneous interfaces investigated in this study contains 8320 atoms and samples the ionic dynamics for times > 10 ns, which enables an accurate assessment of transport properties. Table S6 summarizes the mean absolute errors from the MTP training and its validation.

The calculated D^* as a function of temperature for bulk binary compounds Li_2S , Li_3P and LiCl , with and without Li^+ vacancies (Vac) are shown in Figure 3. We have not included the case of LiCl without vacancies where we could only probe a limited number of diffusion events, which are insufficient to estimate accurate Li-ion diffusivities. The assessment of Li-ion transport in the bulk structures of Li_2S , Li_3P and LiCl is crucial to compare the transport across the heterogeneous interfaces. Notably, our calculated E_a is in reasonable agreement with ex-



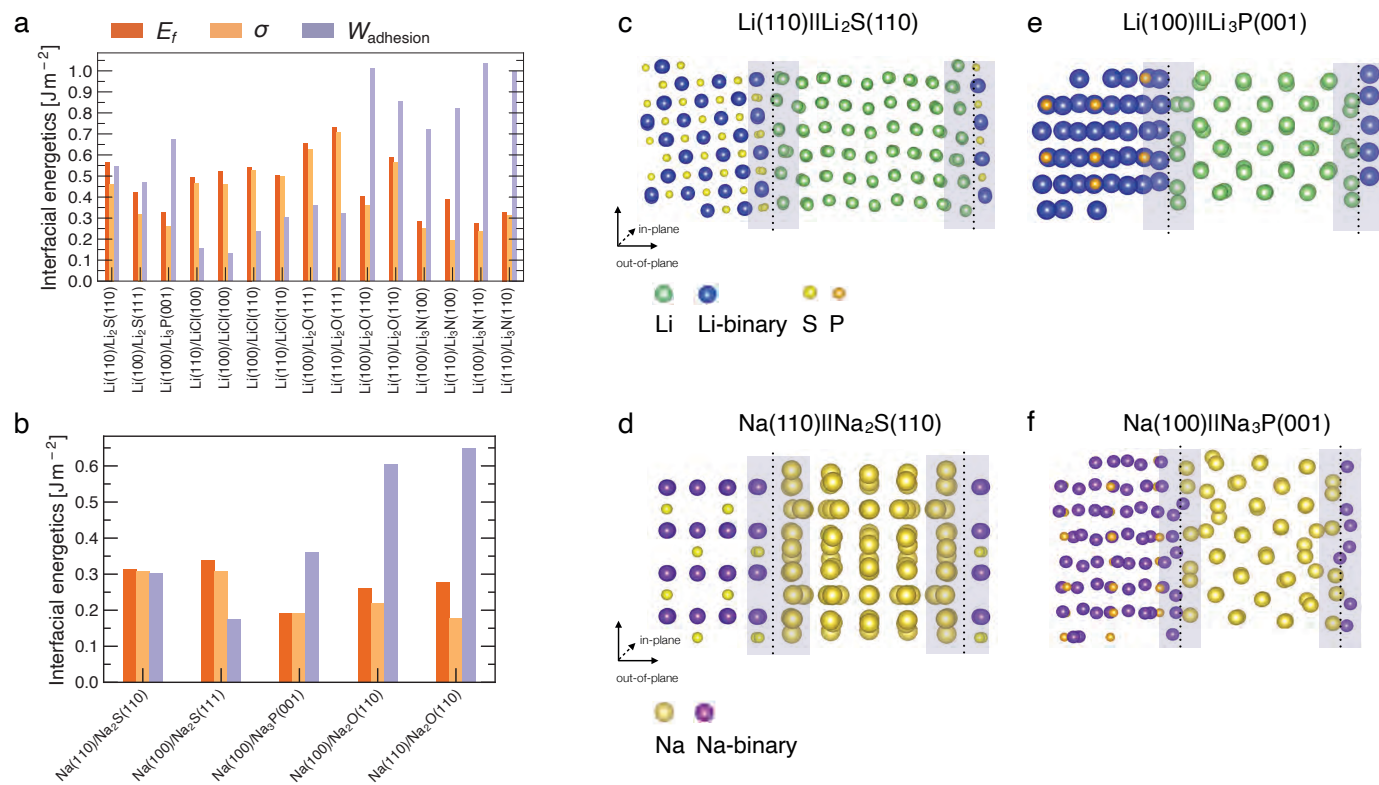


Fig. 2 Computed interfacial quantities (in J m^{-2}) for (a) Li-based interfaces and (b) Na-based interfaces. Atomic structures of representative interfaces, namely (c) $\text{Li}(110)\text{||Li}_2\text{S}(110)$, (d) $\text{Na}(110)\text{||Na}_2\text{S}(110)$ (e) $\text{Li}(100)\text{||Li}_3\text{P}(001)$ and (f) $\text{Na}(100)\text{||Na}_3\text{P}(001)$. The interface regions are indicated by shaded areas. The non-periodic direction of the interface is indicated by the "out-of-plane" vectors.

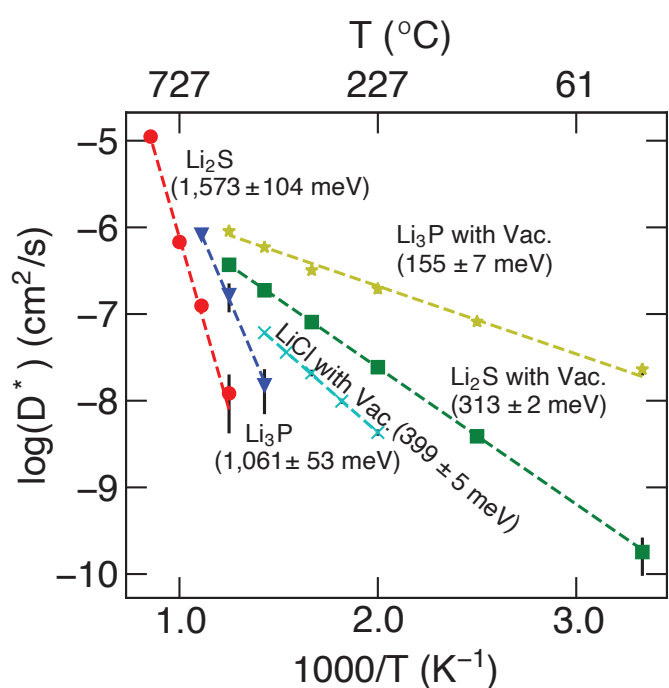


Fig. 3 Arrhenius plots of Li^+ D^* (in $\text{cm}^2 \text{s}^{-1}$) of bulk binary compounds from MTP-MD simulations. The activation energies, calculated from Eq. 7, and the related error bars are provided as text annotations. Vac. stands for structures with a Li-vacancy.

perimental results (see Table S7). For example, the calculated E_a in LiCl with Vac, ($\sim 399 \pm 5$ meV), is qualitatively similar to the existing experimental value (~ 510 meV)⁴⁹. The computed E_a of Li_3P with Vac ($\sim 155 \pm 7$ meV) is in better agreement with experiment (~ 180 meV)⁵⁰ as compared to the pristine Li_3P ($\sim 1061 \pm 53$ meV). On the other hand, the calculated E_a in pristine- Li_2S ($\sim 1573 \pm 104$ meV) is closer to the experimental value (~ 1.5 eV at $T > 800$ K)⁵¹ than the calculated E_a in Li_2S with Vac ($\sim 313 \pm 2$ meV). Unsurprisingly, the introduction of Vac lowers the activation energies of both Li_2S and Li_3P as shown in Figure 3. The calculated E_a of Li_3P (with Vac) is lower than that of Li_2S (with Vac), which is in agreement with previous studies showing superior Li-ion conductivity of Li_3P over Li_2S .⁵²

To investigate the Li-ion transport across the argyrodite- $\text{Li}_6\text{PS}_5\text{Cl}$ | Li-metal interface (i.e., the interfaces formed by the decomposition products of argyrodite with Li metal), we performed MTP-MD simulations on three interface models, namely, $\text{Li}(110)\text{||Li}_2\text{S}(110)$, $\text{Li}(100)\text{||Li}_3\text{P}(001)$ and $\text{Li}(110)\text{||LiCl}(100)$. The choice of these specific interfaces is motivated by their highest W_{adhesion} values (Figure 2a) compared to other possible configurations using Li-metal and the same binary compound. Although $\text{Li}(100)\text{||LiCl}(100)$ has the highest W_{adhesion} , we have chosen $\text{Li}(110)\text{||LiCl}(100)$ as the representative model because of its lower computational cost for AIMD simulations. We randomly introduced a number of Li^+ vacancies ($\sim 1.1\%$) in the interface region to calculate D^* , since it is likely that heterogeneous interfaces will comprise highly defec-

tive materials, especially due to the *in situ* formed decomposition products. To distinguish Li⁺ belonging either to Li-metal or binary compounds, we have labeled Li⁺ in Li-metal as Li⁺(metal) (green spheres in Figure 4, Figure S9), and Li⁺ in binary compounds as Li⁺(binary) (dark blue spheres), respectively. Furthermore, the direction of Li-ion transport with respect to the interfacial plane, i.e., in-plane or out-of-plane, helps to qualify the nature of Li transport. Indeed, only Li-ion diffusing out-of-plane will contribute to effective ion-transport across the interface. The predicted Li⁺- D^* in both Li-metal and binary compounds are summarized in Table S8. The mean square displacement (MSD) plots used to derive the Li⁺- D^* are shown in Figures S11-S13.

In Figure 4a-d and Figure S9a-b, we show the snapshots of different interfaces at 400 K during the MTP-MD simulations. In the following paragraphs, bulk is intended as the portion of the interface model which mimics the bulk structure. Initially, all interfaces exhibit modest atomic rearrangements near the interface region (violet shaded area). After ~5 ns, significant Li⁺ displacement in both the metal and binary bulk along with Li⁺ exchange (i.e., there is a significant amount of Li⁺(metal) diffusing into Li₃P bulk and vice-versa) can be clearly observed in Li(100) || Li₃P(001). This can be understood by the high values of Li⁺- D^* (Figure 4e) in both the in-plane (within bulk systems, 3.03×10^{-6} – 3.76×10^{-6} cm²/s) and out-of-plane (across the bulk systems, 1.93×10^{-7} – 1.99×10^{-7} cm²/s) directions in the Li(100) || Li₃P(001) system.

In contrast, in Li(110) || Li₂S(110) and Li(110) || LiCl(100), we observe limited diffusion events and sparse exchange of Li-ions during the MTP-MDs, which in turn is quantified by the low in-plane (4.86×10^{-8} – 1.89×10^{-7} cm²/s) and even lower out-of-plane (6.43×10^{-9} – 2.21×10^{-8} cm²/s) diffusivities in both systems. We find that for all interfaces, the out-of-plane components of both Li⁺(metal) and Li⁺(binary) are much smaller than their respective in-plane components, which indicate that the Li⁺ diffusion across the interface remains limited.

5 Discussion

A systematic study of the structures, interfacial energetics, and ionic transport properties of solid/solid interfaces is paramount for the development of solid-state batteries. Here, we have used a combination of accurate DFT calculations to explore the stability of interfaces arising from the decomposition of SEs with highly reducing alkali-metals, i.e., Li and Na. Upon identifying the thermodynamically stable heterogeneous interfaces, we trained MTPs based on accurate AIMD simulations, and in turn used such MTPs to run long duration (>10 ns) simulations to elucidate the Li-ion transport properties across specific interfaces.

Although the morphology of real electrode || SE interfaces can be far more complex than the interface models used here, our detailed atomistic models provide insights of the microscopic structure and mechanical stability of buried interfaces between SEs and alkali-metals. Still one major limitation of our analysis is the finite number of interface models considered (20 in this study). Clearly, it is impossible to survey the whole configurational space of interfaces (potentially thousands^{11,16,34}), and alternative strategies should be sought.

This study demonstrates that both surface orientations together with the surface terminations of binary compounds can largely affect the atomistic structures of interfaces (see Section 3), which in turn determine the interfacial lattice coherence, the thermodynamic stability of interfaces and the mechanical stability of such interfaces in LMBs and solid-state batteries. Several studies have revealed the crucial role played by surface terminations of SEs in determining the interfacial stability.^{11,53,54} For example, using first-principles calculations, Tateyama et al⁵³ reported that the low-energy Li₇La₃Zr₂O₁₂ (LLZO) surfaces lead to the chemical instability of LLZO || Li-metal interface.

Our analysis also suggests that W_{adhesion} (of Eq. 4)—measuring the energy cost to separate two materials of a heterogeneous interface—is an important descriptor to evaluate the mechanical stability of interfaces.

In particular, W_{adhesion} should be large enough to avoid interface delamination.⁵⁵ Yang et al. demonstrated that for common Li-metal || SE interfaces, a $W_{\text{adhesion}} > 0.7 \text{ J m}^{-2}$ was required to prevent the formation of interfacial voids with the application of external pressure of 20–30 MPa.²⁹ Recently, Seymour and Aguadero²⁸ have developed a “bond breaking” approach and derived that if $W_{\text{adhesion}} > 2\gamma$ (where γ is the surface energy of Li or Na-metal), the formation of interfacial voids with potential loss of contact during the Li (or Na) stripping could be avoided. Our data suggest that among Li-based interfaces (Table S4), only the Li(100) || Li₂O(110), Li(100) || Li₃N(110) and Li(110) || Li₃N(110) interfaces satisfy this criterion. For interfaces with Na-metal, only the two Na || Na₂O interfaces have a W_{adhesion} larger than twice of the surface energy of Na(110) (or Na(100)).

The mechanisms of LiPON passivation of Li-metal has been a matter of debate.^{23,24,32} Recent studies by Hood et al.²³ have indicated that Li₃N and Li₂O distribute uniformly on the surface of the Li-metal, while Li₃P was not in direct contact with Li-metal. In contrast, the study led by the Meng research group had suggested that only Li₃N, Li₂O and Li₃PO₄ could be present in the interfacial region formed between Li-metal and LiPON.²⁴ Our results show that Li || Li₂O and Li || Li₃N interfaces have better interfacial stabilities than Li || Li₃P, which agree well with the experimental scenario that both Li₂O and Li₃N can be in direct contact with Li-metal, while Li₃P can only exist in the sub-interfacial layer.²³

It has been established that argyrodite SEs are prone to decomposition against Li-metal,^{14,52} with evidence of formation of Li₂S, Li₃P and LiX (with X=Cl, Br or I) at the potential of Li-metal (i.e., 0 Volts vs. Li/Li⁺). Among the interfaces formed between Li-metal and the decomposition products of argyrodite Li₆PS₅Cl as SE, i.e. Li || Li₂S, Li || Li₃P and Li || LiCl, Li || Li₃P has the largest value of W_{adhesion} (Figure 2), suggesting that Li₃P is more likely to form a stable interface with Li-metal as compared to the other binary compounds. On one hand, the appreciable electronic conductivity of Li₃P could lead to continuous reactions with Li-metal and growth of the decomposing interphases.⁵⁶ On the other hand, we have not considered the interfacial stability between binary compounds and Li₆PS₅Cl. Because these interfaces may not be mechanically stable, loss of contact between the SE and its decomposition products may also contribute to increased impedance.^{14,22} Indeed, it has been shown that the



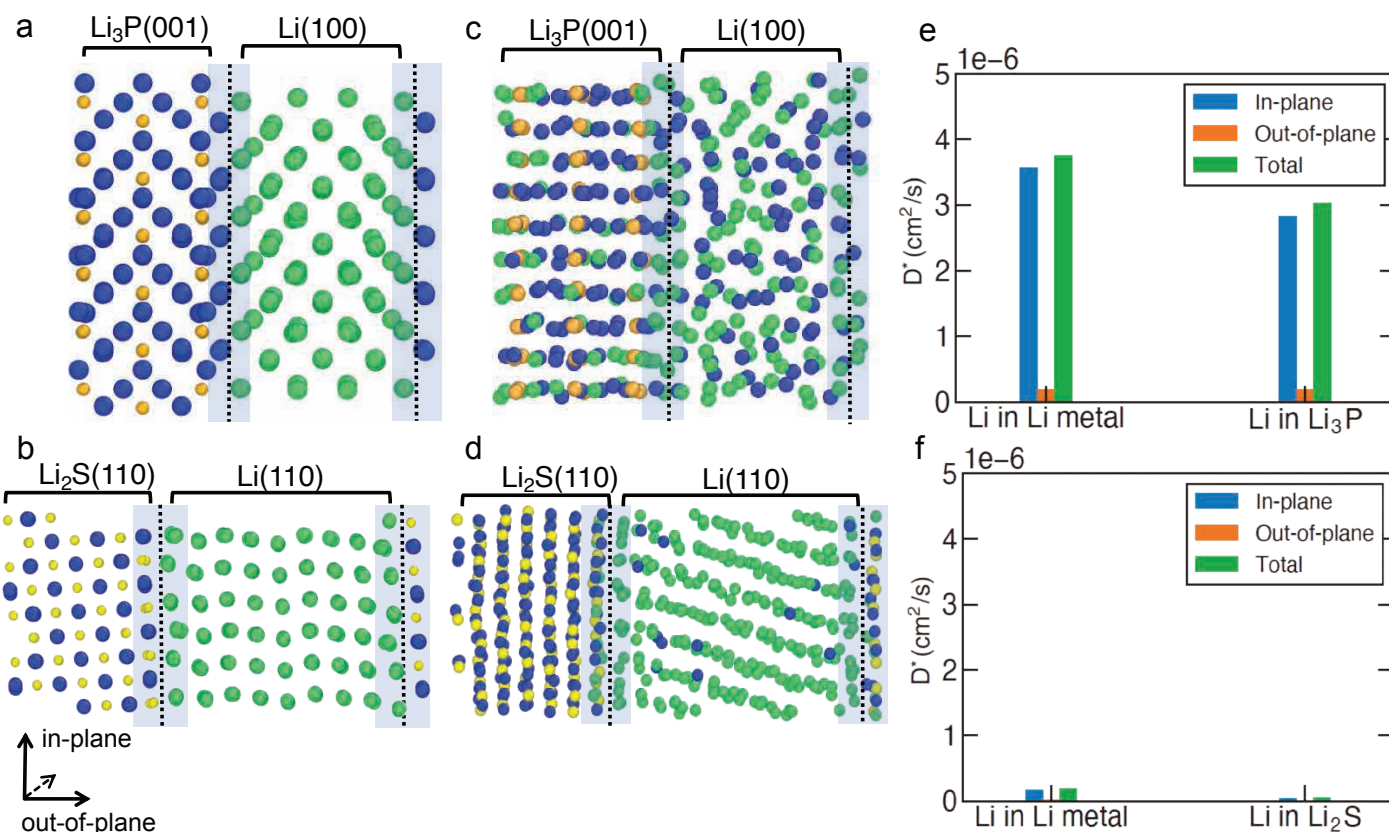


Fig. 4 Snapshots of (a, c) Li(100)||Li₃P(001) and (b, d) Li(110)||Li₂S(110) interfaces at 0 ns (a and b), and 5 ns (c and d), respectively, at 400 K. The in-plane and out-of-plane components of Li⁺-D* in the Li-metal and Li₃P regions (e) of Li(100)||Li₃P(001) interface and Li₂S regions (f) of Li(110)||Li₂S(110) interface at 400 K. Dark blue spheres: Li⁺ (binary), green spheres: Li⁺(metal), orange spheres: P and yellow spheres: S.

change in particle size of Li₂S upon lithiation leads to loss of contact of the Li₆PS₅Cl|Li₂S interface and increases resistance.²⁵

The Li⁺ conductivity (or diffusivity) determined in experiments largely depends on the sample quality, its crystallinity and experimental conditions. In particular, the presence of defects, grain boundaries, and lattice disorder all affect the Li⁺ transport significantly.^{57,58} Therefore, here we have restricted our study to the crystalline structures (both decomposing products and interfaces), a situation where the MTP approach has been proven to be adequate to predict ionic transport properties.^{52,59,60} However, one major limitation of the current implementation of MTP is its lack of transferability from training within the binary bulk systems to being directly used in heterogeneous interfaces, requiring significant retraining of MTP with new training sets for each distinct interface. Therefore, a complete retraining of the MTP for each interface combination considered in this work is highly resource intensive, which pushes a comprehensive examination of Li (and Na) transport across all interfaces out of the scope of our work.

Assume that Li₆PS₅Cl reacts entirely with Li-metal (at 0 Volts vs. Li/Li⁺) according to Eq. 8:^{14,15,52}



where Li₂S is produced 5× in excess over the other binaries,

in agreement with experimental evidences.^{14,22} For example, from X-ray photoemission spectroscopy (XPS) experiments, Wenzel *et al.*¹⁴ and Schwietert *et al.*²² have observed the presence of Li₂S, LiCl, and Li₃P at the argyrodite||Li-metal interface. On the basis of our interfacial energetics, Li⁺ transport calculations and Eq. 8, we propose a macroscopic picture of the interface of decomposing argyrodite-Li₆PS₅Cl against Li-metal, as shown in Figure 5.

Our data suggests a lower stability of LiCl||Li-metal interface as compared to Li₃P and Li₂S, which indicates that LiCl may be in direct contact with Li-metal over a negligible interfacial area. It appears that LiCl may not be directly involved in interfacial Li-transport. At voltages larger than 0.0 Volts vs. Li/Li⁺ other decomposition products have been reported and observed, with the most prominent being Li₃PS₄,^{15,20,22} which may form in the sub-interfacial layers of the SE. Since Li₂S is in molar excess over Li₃P and LiCl, the Li-ion percolation in the proximity of the metal electrode||SE interfaces will be largely limited by the lower ionic conductivity of Li₂S.¹⁴ Furthermore, our explicit study on interfaces confirmed that only Li-metal||Li₃P displays facile Li-ion transport (Figure 4c) as signified by the black arrows in Figure 5. While the interfaces of Li-metal with Li₂S and LiCl are resistive to Li-ion transport (Figure 4, Figure S9). Therefore, our qualitative results suggest that the decomposing interfaces are resistive to Li-ion transport as compared to the unreacted argyrodite SE.¹⁴ Note

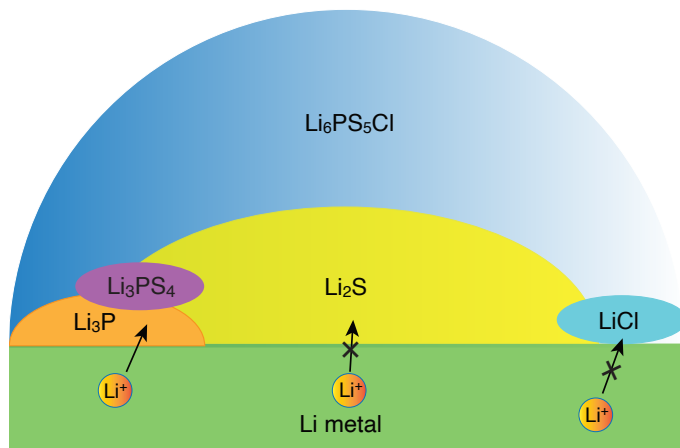


Fig. 5 Schematic illustration of a possible structure of the interface between Li-metal and argyrodite- $\text{Li}_6\text{PS}_5\text{Cl}$, as inferred from the interfacial energetics and Li-ion transport simulations.

that the interfaces formed among different decomposition products (e.g., $\text{Li}_3\text{P} \parallel \text{Li}_2\text{S}$) or the decomposition products with the solid electrolyte (e.g., $\text{Li}_6\text{PS}_5\text{Cl}$) are also of crucial importance to Li-ion transport. Therefore, explicit studies of these interfaces using high-fidelity machine learned potentials are certainly needed.

6 Conclusion

Chalcogen-containing SEs show among the highest room temperature ionic conductivities ($\sim 10^{-2} \text{ S cm}^{-1}$), but their practical applications in LMBs are limited by the decomposing interfaces when in contact with Li metal. Similar constraints bottleneck the implementation of SEs in NIBs as well. Therefore, it is vital to understand the interfacial properties of these decomposing interfaces, either experimentally or theoretically. In this work, we have systematically evaluated the thermodynamic stability (of Li- and Na-systems) and Li-ion transport properties of multiple decomposing interfaces, by employing first-principles calculations and large-scale MD simulations based on MLPs. Our results reveal that the interfacial stability of decomposition products with alkali-metals is largely affected by the surface properties of the decomposition products. In general, we have observed that the interfaces formed between alkali-metal with argyrodite- $\text{Li}_6\text{PS}_5\text{Cl}$ are resistive, to Li-ion transport. Finally, our high-fidelity MLPs, trained explicitly for interfaces, shed light on the complicated interfacial transport properties, which will aid in the study and optimization of SEs in the future.

7 Methods

7.1 First-principles Calculations

DFT was used to approximate the energy contributions introduced in Sec. 2. The wavefunctions were described using plane-waves for the valence electrons together with projected augmented wave potentials for the core electrons as implemented in the Vienna Ab-initio Simulation Package (VASP).^{61–63} The exchange-correlation contributions were treated within the generalized gradient approximation (GGA) as parameterized by Perdew, Burke, and Ernzerhof (PBE).⁶⁴ The valence electron con-

figurations for each element were as follows: Li: $s^1 p^0$, N: $s^2 p^3$, O: $s^2 p^4$, Na: $s^1 p^0$, P: $s^2 p^3$, S: $s^2 p^4$ and Cl: $s^2 p^5$. The parameters we used for geometry optimization, surface energy and interfacial energetics calculations of the binary compounds and the constructed interfaces follow the MITRelaxSet, as in pymatgen.⁶⁵ We used a plane wave energy cutoff of 520 eV and a k -point mesh generated using a k -point density of 25 \AA^{-1} . The total energy of each structure was converged to 10^{-5} eV/cell , and the geometry optimizations were stopped when the change in total energy was smaller than 10^{-4} eV between two subsequent ionic steps.

AIMD were performed with VASP to generate the initial training sets for the MTP-MD (see Sec. 7.2). A plane-wave energy cutoff of 400 eV and a Γ -only k -mesh were used. The canonical ensemble (NVT) was achieved using Nosé-Hoover thermostat and a time step of 2 fs.^{66,67} Since previous studies have reported^{59,68} that the training set for MTP-MD should cover the whole configurational space and contain sufficient data so as to rarely invoke DFT calculations, we performed AIMD calculations at 1000 K for 14–20 ps (preceded by a temperature ramping of 2 ps), which resulted in training sets containing 7000–10000 configurations. The supercell sizes used for binary compounds pristine structures were $4 \times 4 \times 4$ for Li metal (128 atoms), $2 \times 2 \times 2$ for Li_2S (96 atoms), $3 \times 3 \times 3$ for Li_3P (216 atoms) and $3 \times 3 \times 3$ for LiCl (216 atoms). We also studied the vacancy-mediated diffusion by creating Li^+ vacancies inside the Li metal and binary compounds.

Li^+ vacancies were introduced by removing Li atoms and compensating with a uniform (jellium) charge background. Also, we created specific supercells that enabled a Li^+ vacancy concentration of $\sim 0.8\%$ for all compounds, which can arise at a synthesis temperature of 1200 K with a defect formation energy of 0.5 eV. Specifically, we used supercells of $4 \times 4 \times 4$ with one Li^+ vacancy for Li metal (127 atoms), $2 \times 2 \times 4$ with one Li^+ vacancy for Li_2S (191 atoms), $3 \times 3 \times 3$ with one Li^+ vacancy for Li_3P (215 atoms) and $3 \times 3 \times 3$ with one Li^+ vacancy for LiCl (215 atoms). To study the Li^+ transport across Li-metal || decomposition product interfaces, we have created Li^+ vacancies randomly in the interface region (shaded regions in Figures 2 and 4, with a vacancy concentration of $\sim 1.1\%$). The interfaces that we chose were $\text{Li}(110) \parallel \text{Li}_2\text{S}(110)$ (520 atoms), $\text{Li}(100) \parallel \text{Li}_3\text{P}(001)$ (406 atoms) and $\text{Li}(110) \parallel \text{LiCl}(100)$ (439 atoms).

7.2 Moment-Tensor Potential Molecular Dynamics

MTP for bulk and interfaces investigated in this study were trained using the machine learning of interatomic potentials (MLIP) package.⁶⁹ In the training of the MTP potentials, several parameters need to be carefully selected to balance computational cost vs. accuracy of the trained potentials. During training, we have extensively tested the effects of weights on reproducing the *ab initio* total energies, forces and stresses, as well as cutoff radius (Rcut) and the maximum level of basis functions (lev_{max}) on the accuracy of energy and forces of trained MTP potentials. We concluded that a ratio of weights of 100:10:1 for energies, forces, and stresses, respectively, was appropriate to achieve good accuracy. Also, we found that a lev_{max} of 10 and a Rcut of 5 Å, provided a tolerable level of fitting and validation errors in ener-

gies (< 10 meV/atom) and forces (< 30 meV/Å), as documented in Table S6.

Since our MTPs were trained at high temperatures (~1000 K), we further validated the transferability of the potentials to lower temperatures (i.e., 300–500 K). Specifically, we constructed validation sets by performing AIMD at 300 K/500 K for 4 ps (~2000 snapshots for each temperature). The fitting and validation errors on the total energies in both binary compounds and interface models were always < 10 meV, while the errors on forces were within ~30 meV Å⁻¹.

Upon training, MTP-MD were performed using LAMMPS,⁷⁰ where the MD simulations were performed in the temperature range of 300–1000 K at intervals of 100 K. A Nosé-Hoover thermostat was used to simulate the canonical ensemble (NVT).^{66,67} Long MD simulations were carried out for at least 10 ns with a short timestep of 1 fs, preceded by a temperature ramping for 100 ps and an equilibration period of 1 ns to reach each target temperature. We also benchmarked our MTP D^* data with AIMD results (see Table S9). Specifically, we find that our MTP-MD calculated D^* at 900 K and 800 K are in reasonable agreement with AIMD calculations at the same temperatures, signifying the high fidelity of our MTP-MD simulations. The trained moment tensor potentials for both binary compounds and interface models are publicly available in the repository https://github.com/caneparesearch/MTP-Li_interface_binaries.git.

7.3 Error analysis of lithium ion diffusivity

To attain a better estimate of the computed Li-ion diffusivity and activation energy, we have considered the statistical variance of tracer diffusivity, $D^*(T)$ and performed a weighted linear least squares regression, following He et al methodology.⁷¹ In our Arrhenius plot, the weight of each point is determined by the reciprocal of the variance of $\log D^*(T)$. The variance of $\log D^*(T)$ is calculated based on the propagation of uncertainty using Eq. 9:

$$\sigma(\log D^*(T))^2 = \frac{\sigma(D^*(T))^2}{D^*(T)^2} \quad (9)$$

where σ is the standard deviation of $D^*(T)$. We have divided the entire MD simulation into multiple non-overlapping MD sections, from which σ is determined. To minimize σ , we have tried dividing the MD simulations into different number of sections. For example, in LiCl we have computed σ for different number of sections, such as 10 ($\sigma=1.48 \times 10^{-8}$ cm²/s), 100 (2.13×10^{-8}) and 1000 (6.73×10^{-8}). Clearly, larger numbers of section increase σ ; in this study, we have chosen 10 sections.

7.4 Validation of Interfacial Models

To verify the accuracy of our methodology in predicting interfacial properties, we have calculated interfacial energetics using two additional “constrained” optimization methods, namely, i) “Fix-binary”: the middle layers of the decomposition product was fixed to mimic the bulk in-plane lattice constants of the binary compound, and, ii) “Fix-metal”: middle layers of Li(Na) metal are fixed. The default method used throughout the work is when we do not constrain the middle layers of either binary

compounds or the metal, referred to as “Fully-relaxed”. To test these scenarios, we chose Na(110) || Na₂O(110) for Na-based and Li(100) || Li₃P(001) for Li-based interfaces, respectively. The calculated E_f , with and without constrained optimization, are shown in Figure S6. Notably, E_f calculated using constrained optimization is ~0.02 J m⁻² and ~0.1 J m⁻² higher than Fully-relaxed for Li(100) || Li₃P(001), and Na(110) || Na₂O(110), respectively.

Another typically used approach for calculating interfacial energy σ excluding the strain effect is to compute interface formation energy at varied slab thickness of Li(or Na)-metal, and σ is obtained by taking the y-intercept of the extrapolated value of E_f .²⁶ To test this approach, we have taken Li(100) || Li₃P(001) and Li(110) || Li₂S interfaces which are used later to investigate Li-ion transport. We fixed the in-plane lattice constants of the interfaces to that of the binary compounds, while varying the number of Li-metal slabs. We find that in both cases, the variations of E_f with different formula units of Li-metal slab (denoted as n_{Li}) are not significant (see Figure S10). This indicates that the strain energy is not very sensitive to the system size. Using both approaches, the Li(100) || Li₃P(001) interface appears consistently more stable than the Li(110) || Li₂S interface.

Acknowledgement

J.W. A.A.P. and P.C. acknowledges funding from the National Research Foundation under his NRF Fellowship NRFF12-2020-0012. The computational work was performed on resources of the National Supercomputing Centre, Singapore (<https://www.nscc.sg>).

Notes and references

- 1 J. B. Goodenough and Y. Kim, *Chem. Mater.*, 2010, **22**, 587–603.
- 2 W. Xu, J. Wang, F. Ding, X. Chen, E. Nasybulin, Y. Zhang and J.-G. Zhang, *Energy Environ. Sci.*, 2014, **7**, 513–537.
- 3 D. Lin, Y. Liu and Y. Cui, *Nature Nanotech.*, 2017, **12**, 194–206.
- 4 T. Krauskopf, F. H. Richter, W. G. Zeier and J. Janek, *Chem. Rev.*, 2020, **120**, 7745–7794.
- 5 X.-B. Cheng, R. Zhang, C.-Z. Zhao and Q. Zhang, *Chem. Rev.*, 2017, **117**, 10403–10473.
- 6 C. Fang, B. Lu, G. Pawar, M. Zhang, D. Cheng, S. Chen, M. Ceja, J.-M. Doux, H. Musrock, M. Cai, B. Liaw and Y. S. Meng, *Nat Energy*, 2021, **6**, 987–994.
- 7 K. Xu, *Chem. Rev.*, 2004, **104**, 4303–4418.
- 8 N. Yabuuchi, K. Kubota, M. Dahbi and S. Komaba, *Chem. Rev.*, 2014, **114**, 11636–11682.
- 9 P. K. Nayak, L. Yang, W. Brehm and P. Adelhelm, *Angew. Chem. Int. Ed.*, 2018, **57**, 102–120.
- 10 C. Delmas, *Adv. Energy Mater.*, 2018, **8**, 1703137.
- 11 J. Haruyama, K. Sodeyama, L. Han, K. Takada and Y. Tateyama, *Chem. Mater.*, 2014, **26**, 4248–4255.
- 12 H. Tang, Z. Deng, Z. Lin, Z. Wang, I.-H. Chu, C. Chen, Z. Zhu, C. Zheng and S. P. Ong, *Chem. Mater.*, 2018, **30**, 163–173.
- 13 E. A. Wu, C. S. Kompella, Z. Zhu, J. Z. Lee, S. C. Lee, I.-H.



- Chu, H. Nguyen, S. P. Ong, A. Banerjee and Y. S. Meng, *ACS Appl. Mater. Interfaces*, 2018, **10**, 10076–10086.
- 14 S. Wenzel, S. J. Sedlmaier, C. Dietrich, W. G. Zeier and J. Janek, *Solid State Ionics*, 2018, **318**, 102–112.
- 15 W. D. Richards, L. J. Miara, Y. Wang, J. C. Kim and G. Ceder, *Chem. Mater.*, 2016, **28**, 266–273.
- 16 B. Gao, R. Jalem and Y. Tateyama, *ACS Appl. Mater. Interfaces*, 2021, **13**, 11765–11773.
- 17 T. Famprakis, P. Canepa, J. A. Dawson, M. S. Islam and C. Masquelier, *Nat. Mater.*, 2019, **18**, 1278–1291.
- 18 T. Famprakis, Ö. U. Kudu, J. A. Dawson, P. Canepa, F. Fauth, E. Suard, M. Zbiri, D. Dambouronet, O. J. Borkiewicz, H. Bouyanif, S. P. Emge, S. Cretu, J.-N. Chotard, C. P. Grey, W. G. Zeier, M. S. Islam and C. Masquelier, *J. Am. Chem. Soc.*, 2020, **142**, 18422–18436.
- 19 L. Baggetto, R. A. H. Niessen, F. Roozeboom and P. H. L. Notten, *Adv. Funct. Mater.*, 2008, **18**, 1057–1066.
- 20 Y. Zhu, X. He and Y. Mo, *J. Mater. Chem. A*, 2016, **4**, 3253–3266.
- 21 V. Lacivita, Y. Wang, S.-H. Bo and G. Ceder, *J. Mater. Chem. A*, 2019, **7**, 8144–8155.
- 22 T. K. Schwietert, V. A. Arszelewska, C. Wang, C. Yu, A. Vasileiadis, N. J. J. de Klerk, J. Hageman, T. Hupfer, I. Kerkamm, Y. Xu, E. van der Maas, E. M. Kelder, S. Ganapathy and M. Wagemaker, *Nat. Mater.*, 2020, **19**, 428–435.
- 23 Z. D. Hood, X. Chen, R. L. Sacci, X. Liu, G. M. Veith, Y. Mo, J. Niu, N. J. Dudney and M. Chi, *Nano Lett.*, 2021, **21**, 151–157.
- 24 D. Cheng, T. A. Wynn, X. Wang, S. Wang, M. Zhang, R. Shimizu, S. Bai, H. Nguyen, C. Fang, M.-c. Kim, W. Li, B. Lu, S. J. Kim and Y. S. Meng, *Joule*, 2020, **4**, 2484–2500.
- 25 C. Yu, S. Ganapathy, N. J. J. de Klerk, I. Roslon, E. R. H. van Eck, A. P. M. Kentgens and M. Wagemaker, *J. Am. Chem. Soc.*, 2016, **138**, 11192–11201.
- 26 N. D. Lepley and N. A. W. Holzwarth, *Phys. Rev. B*, 2015, **92**, 214201.
- 27 C.-T. Yang and Y. Qi, *Chem. Mater.*, 2021, **33**, 2814–2823.
- 28 I. D. Seymour and A. Aguadero, *J. Mater. Chem. A*, 2021, 10.1039/D1TA03254B.
- 29 M. Yang, Y. Liu, A. M. Nolan and Y. Mo, *Adv. Mater.*, 2021, **33**, 2008081.
- 30 F. Mizuno, A. Hayashi, K. Tadanaga and M. Tatsumisago, *Adv. Mater.*, 2005, **17**, 918–921.
- 31 T. Hakari, M. Nagao, A. Hayashi and M. Tatsumisago, *Journal of Power Sources*, 2015, **293**, 721–725.
- 32 A. Schwöbel, R. Hausbrand and W. Jaegermann, *Solid State Ionics*, 2015, **273**, 51–54.
- 33 P. W. Tasker, *J. Phys. C: Solid State Phys.*, 1979, **12**, 4977–4984.
- 34 K. T. Butler, G. Sai Gautam and P. Canepa, *npj Comput Mater*, 2019, **5**, 19.
- 35 T. Einstein, *Handbook of Crystal Growth*, Elsevier, 2015, pp. 215–264.
- 36 R. Tran, Z. Xu, B. Radhakrishnan, D. Winston, W. Sun, K. A. Persson and S. P. Ong, *Sci Data*, 2016, **3**, 160080.
- 37 Y.-X. Chen and P. Kagazchi, *Nanoscale*, 2014, **6**, 13391–13395.
- 38 W. C. Mackrodt, *J. Chem. Soc., Faraday Trans. 2*, 1989, **85**, 541.
- 39 Z. Liu, Y. Qi, Y. X. Lin, L. Chen, P. Lu and L. Q. Chen, *J. Electrochem. Soc.*, 2016, **163**, A592–A598.
- 40 A. Hashibon, C. Elsasser and M. Ruhle, *Acta Materialia*, 2005, **53**, 5323–5332.
- 41 R. Benedek, D. N. Seidman and C. Woodward, *J. Phys.: Condens. Matter*, 2002, **14**, 2877–2900.
- 42 A.-L. Dalverny, J.-S. Filhol and M.-L. Doublet, *J. Mater. Chem.*, 2011, **21**, 10134.
- 43 N. T. Taylor, F. H. Davies, I. E. M. Rudkin, C. J. Price, T. H. Chan and S. P. Hepplestone, *Computer Physics Communications*, 2020, **257**, 107515.
- 44 Z. Deng, Z. Wang, I.-H. Chu, J. Luo and S. P. Ong, *J. Electrochem. Soc.*, 2016, **163**, A67–A74.
- 45 A. Kato, H. Kowada, M. Deguchi, C. Hotehama, A. Hayashi and M. Tatsumisago, *Solid State Ionics*, 2018, **322**, 1–4.
- 46 Y. Xiao, Y. Wang, S.-H. Bo, J. C. Kim, L. J. Miara and G. Ceder, *Nat Rev Mater*, 2020, **5**, 105–126.
- 47 J. Bates, *Solid State Ionics*, 1992, **53–56**, 647–654.
- 48 A. V. Shapeev, *Multiscale Model. Simul.*, 2016, **14**, 1153–1173.
- 49 R. Court-Castagnet, *Solid State Ionics*, 1993, **61**, 327–334.
- 50 G. Nazri, *Solid State Ionics*, 1989, **34**, 97–102.
- 51 F. Altorfer, W. Bührer, I. Anderson, O. Schärf, H. Bill, P. Carron and H. Smith, *Physica B: Condensed Matter*, 1992, **180–181**, 795–797.
- 52 C. Wang, K. Aoyagi, M. Aykol and T. Mueller, *ACS Appl. Mater. Interfaces*, 2020, **12**, 55510–55519.
- 53 B. Gao, R. Jalem and Y. Tateyama, *ACS Appl. Mater. Interfaces*, 2020, **12**, 16350–16358.
- 54 H.-K. Tian, R. Jalem, B. Gao, Y. Yamamoto, S. Muto, M. Sakakura, Y. Iriyama and Y. Tateyama, *ACS Appl. Mater. Interfaces*, 2020, **12**, 54752–54762.
- 55 A. Wang, S. Kadam, H. Li, S. Shi and Y. Qi, *npj Comput Mater*, 2018, **4**, 15.
- 56 P. Gorai, T. Famprakis, B. Singh, V. Stevanović and P. Canepa, *Chem. Mater.*, 2021, **33**, 7484–7498.
- 57 V. Lacivita, N. Artrith and G. Ceder, *Chem. Mater.*, 2018, **30**, 7077–7090.
- 58 E. Sebti, H. A. Evans, H. Chen, P. M. Richardson, K. M. White, R. Giovine, K. P. Koirala, Y. Xu, E. Gonzalez-Correia, C. Wang, C. M. Brown, A. K. Cheetham, P. Canepa and R. J. Clément, 2022.
- 59 C. Wang, K. Aoyagi, P. Wisesa and T. Mueller, *Chem. Mater.*, 2020, **32**, 3741–3752.
- 60 J. Qi, S. Banerjee, Y. Zuo, C. Chen, Z. Zhu, M. Holekevi Chandrappa, X. Li and S. Ong, *Materials Today Physics*, 2021, **21**, 100463.
- 61 P. E. Blöchl, *Phys. Rev. B*, 1994, **50**, 17953–17979.
- 62 G. Kresse and D. Joubert, *Phys. Rev. B*, 1999, **59**, 1758–1775.



- 63 G. Kresse and J. Furthmüller, *Phys. Rev. B*, 1996, **54**, 11169–11186.
- 64 J. P. Perdew, K. Burke and M. Ernzerhof, *Phys. Rev. Lett.*, 1996, **77**, 3865–3868.
- 65 S. P. Ong, W. D. Richards, A. Jain, G. Hautier, M. Kocher, S. Cholia, D. Gunter, V. L. Chevrier, K. A. Persson and G. Ceder, *Computational Materials Science*, 2013, **68**, 314–319.
- 66 S. Nosé, *The Journal of Chemical Physics*, 1984, **81**, 511–519.
- 67 W. G. Hoover, *Phys. Rev. A*, 1985, **31**, 1695–1697.
- 68 I. Novoselov, A. Yanilkin, A. Shapeev and E. Podryabinkin, *Computational Materials Science*, 2019, **164**, 46–56.
- 69 E. V. Podryabinkin and A. V. Shapeev, *Computational Materials Science*, 2017, **140**, 171–180.
- 70 S. Plimpton, *Journal of Computational Physics*, 1995, **117**, 1–19.
- 71 X. He, Y. Zhu, A. Epstein and Y. Mo, *npj Comput Mater*, 2018, **4**, 18.

